

# SPDIM: SOURCE-FREE UNSUPERVISED CONDITIONAL AND LABEL SHIFTS ADAPTATION IN EEG

**Shanglin Li<sup>1,2,†</sup>, Motoaki Kawanabe<sup>2,3</sup> & Reinmar J. Kobler<sup>2,3,†</sup>**

<sup>1</sup> Nara Institute of Science and Technology (NAIST), Nara, Japan

<sup>2</sup> Department of Dynamic Brain Imaging, ATR, Kyoto, Japan

<sup>3</sup> Center for Advanced Intelligence Project, RIKEN, Tokyo, Japan

† Equal contribution

{shanglin, kawanabe, reinmar.kobler}@atr.jp

## ABSTRACT

The non-stationary nature of electroencephalography (EEG) introduces distribution shifts across domains (e.g., days and subjects), posing a significant challenge to EEG-based neurotechnology generalization. Without labeled calibration data for target domains, the problem is a source-free unsupervised domain adaptation (SFUDA) problem. For scenarios with constant label distribution, Riemannian geometry-aware statistical alignment frameworks on the symmetric positive definite (SPD) manifold are considered state-of-the-art. However, many practical scenarios, including EEG-based sleep staging, exhibit label shifts. Here, we propose a geometric deep learning framework for SFUDA problems under specific distribution shifts, including label shifts. We introduce a novel, realistic generative model and show that prior Riemannian statistical alignment methods on the SPD manifold can compensate for specific marginal and conditional distribution shifts but hurt generalization under label shifts. As a remedy, we propose a parameter-efficient manifold optimization strategy termed SPDIM. SPDIM uses the information maximization principle to learn a single SPD-manifold-constrained parameter per target domain. In simulations, we demonstrate that SPDIM can compensate for the shifts under our generative model. Moreover, using public EEG-based brain-computer interface and sleep staging datasets, we show that SPDIM outperforms prior approaches.

## 1 INTRODUCTION

Electroencephalography (EEG) measures multi-channel electric brain activity from the human scalp (Niedermeyer & da Silva, 2005) and can reveal cognitive processes (Pfurtscheller & Da Silva, 1999), emotion states (Suhaimi et al., 2020), and health status (Alotaiby et al., 2014). Neurotechnology and brain-computer interfaces (BCI) aim to extract patterns from the EEG activity that can be utilized for various applications, including rehabilitation and communication (Wolpaw et al., 2002). Despite their capabilities, they currently suffer from a low signal-to-noise ratio, low specificity, and non-stationarities manifesting as distribution shifts across days and subjects (Fairclough & Lotte, 2020).

For EEG-based neurotechnology, distribution shifts have been traditionally mitigated by collecting labeled calibration data and training domain-specific models (Lotte et al., 2018), limiting neurotechnology utility and scalability (Wei et al., 2022). As an alternative, domain adaptation (DA) learns a model from one or multiple source domains that performs well on different (but related) target domain(s), offering principled statistical learning approaches with theoretical guarantees (Ben-David et al., 2010; Hoffman et al., 2018). Within the BCI field, DA primarily addresses cross-session and cross-subject transfer learning (TL) problems (Wu et al., 2020), aiming to achieve robust generalization across domains (e.g., sessions and subjects) without supervised calibration data.

BCIs that generalize across domains without requiring labeled calibration data are one of the grand challenges in EEG-based BCI research (Fairclough & Lotte, 2020; Wolpaw et al., 2002). Since target domain data is typically not available during training, the problem corresponds to a source-free unsupervised domain adaptation (SFUDA) problem (Liu et al., 2021; Yang et al., 2021). For

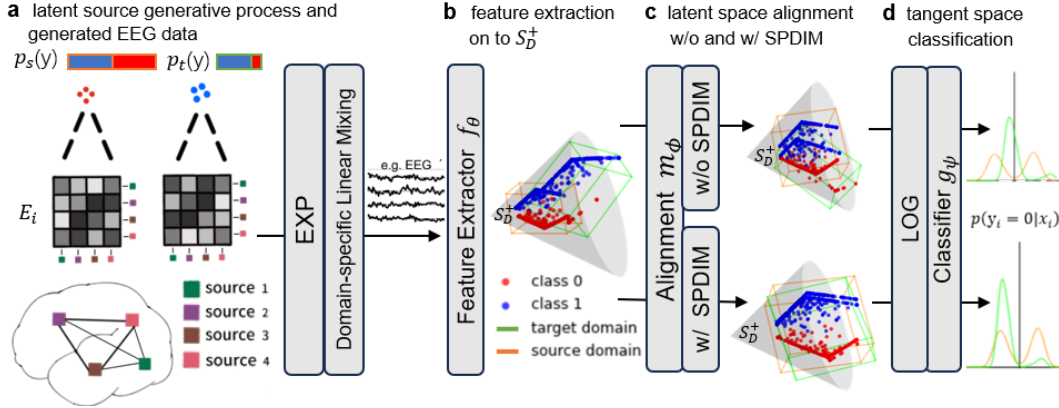


Figure 1: **Visualization of SPDIM framework.** **a**, EEG data is obtained by a domain-specific linear mixing from source signals. **b**, visualization of the latent representations learned by the feature extractor. **c**, visualization of the latent alignment without (top) and with (bottom) SPDIM under label shifts. **d**, density plots show that SPDIM better aligns the distribution.

this problem class, Riemannian geometry-aware statistical alignment frameworks (Barachant et al., 2011) operating with symmetric, positive definite (SPD) matrix-valued features are considered state-of-the-art (SoA) in cross-domain (Roy et al., 2022; Mellot et al., 2023) generalization. They offer several advantageous properties, including invariance to linear mixing, that are suitable for EEG data (Congedo et al., 2017). Additionally, prior works proposed consistent (Sabbagh et al., 2020) and inherently interpretable (Kobler et al., 2021) estimators for generative models with a log-linear relationship between the power of latent sources and the labels. To facilitate generalization across domains, statistical alignment frameworks aim to align first (Zanini et al., 2017; Yair et al., 2019) and second (Rodrigues et al., 2019; Kobler et al., 2022a) order moments, denoted Fréchet mean and variance on Riemannian manifolds. Once the moments are aligned, a model trained on source domains typically generalizes to related target domains (Zanini et al., 2017; Wei et al., 2022; Kobler et al., 2022a; Mellot et al., 2024).

Although infrequently studied, many applications, including EEG-based sleep staging, exhibit label shifts (Thölke et al., 2023). Under label shifts, aligning the moments of the marginal feature distributions can increase the generalization error (Bakas et al., 2023). To address various sources of distribution shifts in EEG, an SFUDA approach that can deal with additional label shifts is required. Machine learning literature offers several frameworks for SFUDA problems with label shifts (Li et al., 2021; Liang et al., 2024), but few have been applied to EEG data. For example, Li et al. (2023) employed the information maximization (Shi & Sha, 2012) objective for cross-domain generalization. Within Riemannian geometry methods, Mellot et al. (2024) studied an EEG-based age regression problem and proposed a framework to facilitate generalization across populations with different prior distributions.

Here, we propose a geometric deep learning framework to tackle SFUDA classification problems under distribution shifts, including label shifts. We introduce a realistic generative model with a log-linear relationship between the covariance of latent sources and the labels (Figure 1a). We provide theoretical analyses showing that prior Riemannian statistical alignment methods on the SPD manifold can compensate for the conditional distribution shifts introduced in our model but hurt generalization under additional label shifts (Figure 1b, c (top)). As a remedy, we propose a parameter-efficient manifold optimization strategy termed SPDIM. SPDIM employs the information maximization principle to learn a domain-specific SPD-manifold-constrained bias parameter to compensate over-corrections introduced via aligning the Fréchet mean (Figure 1b, c (bottom)).

## 2 PRELIMINARIES

### 2.1 SFUDA SCENARIO

Let  $y$  and  $x$  denote random variables representing the true labels and associated features, and let  $p_j(y)$  and  $p_j(x|y)$  be the prior and conditional probability distributions for domain  $j$ . In the transfer learning scenario considered here, we assume that the class priors  $p_j(y)$  can be different from each other, as well as specific shifts in the conditional distributions  $p_j(x|y)$ . We consider a labeled source dataset  $\mathcal{D}_s = \{(x_i, y_i, j_i) | x_i \in \mathcal{X}_s, y_i \in \mathcal{Y}_s, j_i \in \mathcal{J}_s\}_{i=1}^{L_s}$  and an unlabeled target dataset  $\mathcal{D}_t = \{(x_i, j_i) | x_i \in \mathcal{X}_t, y_i \in \mathcal{Y}_t, j_i \in \mathcal{J}_t\}_{i=1}^{L_t}$ , where  $y_i$  and  $j_i$  (or  $j(i)$  if used as suffix) indicate the associated label and domain for each example  $i$ . We additionally assume that both datasets share the feature space (i.e.,  $\mathcal{X}_s = \mathcal{X}_t = \mathcal{X}$ ), contain the same classes (i.e.,  $\mathcal{Y}_s = \mathcal{Y}_t = \mathcal{Y}$ ), and comprise examples from different domains (i.e.,  $\mathcal{J}_s \cap \mathcal{J}_t = \emptyset$ ). The goal is to transfer the knowledge learned from  $\mathcal{D}_s$  to  $\mathcal{D}_t$  via first learning a source decoder  $h_s$  within hypothesis class  $\mathcal{H}$  and then use  $h_s$  and the unlabeled target dataset  $\mathcal{D}_t$  to learn  $h_t \in \mathcal{H}$ .

### 2.2 RIEMANNIAN GEOMETRY ON $\mathcal{S}_D^+$

The SPD manifold  $\mathcal{S}_D^+ = \{C \in \mathbb{R}^{D \times D} : C^T = C, C \succ 0\}$  together with an inner product on its tangent space  $\mathcal{T}_C \mathcal{S}_D^+$  at each point  $C \in \mathcal{S}_D^+$  forms a Riemannian manifold. Tangent spaces have Euclidean structure with easy-to-compute distances, which locally approximate Riemannian distances on  $\mathcal{S}_D^+$  (Absil et al., 2008). In this work, we consider the affine invariant Riemannian metric (AIRM)  $g_C^{\text{AIRM}}(S_1, S_2) = \text{Tr}(C^{-1}S_1C^{-1}S_2)$  as the inner product, which gives rise to the following distance (Bhatia, 2009):

$$\delta(C_1, C_2) = \|\log(C_1^{-\frac{1}{2}}C_2C_1^{-\frac{1}{2}})\|_F \quad (1)$$

where  $C_1$  and  $C_2$  are two SPD matrices,  $\text{Tr}(\cdot)$  denotes the trace,  $\log(\cdot)$  the matrix logarithm, and  $\|\cdot\|_F$  the Frobenius norm. For a set of points  $\mathcal{C} = \{C_i \in \mathcal{S}_D^+\}_{i \leq M}$ , the Fréchet mean is defined as the minimizer of the average squared distances:

$$\bar{C} = \arg \min_{G \in \mathcal{S}_D^+} \nu_G(\mathcal{C}) = \arg \min_{G \in \mathcal{S}_D^+} \frac{1}{M} \sum_{j=1}^M \delta^2(G, C_j) \quad (2)$$

For  $M = 2$ , there exists a closed form solution:

$$\bar{C} = \arg \min_{G \in \mathcal{S}_D^+} \nu_G(\{C_1, C_2\}) = C_1 \#_t C_2|_{t=\frac{1}{2}} = C_1^{\frac{1}{2}} \left( C_1^{-\frac{1}{2}} C_2 C_1^{-\frac{1}{2}} \right)^t C_1^{\frac{1}{2}} \Big|_{t=\frac{1}{2}} \quad (3)$$

where parameter  $t \in [0, 1]$  smoothly interpolates along the geodesic  $C_1 \#_t C_2$  (i.e., the shortest path) connecting both points.

The logarithmic map  $\text{Log}_{\bar{C}} : \mathcal{S}_D^+ \rightarrow \mathcal{T}_{\bar{C}} \mathcal{S}_D^+$  and exponential map  $\text{Exp}_{\bar{C}} : \mathcal{T}_{\bar{C}} \mathcal{S}_D^+ \rightarrow \mathcal{S}_D^+$  project points between the manifold and the tangent space at point  $\bar{C}$ :

$$\text{Log}_{\bar{C}}(C_i) = \bar{C}^{\frac{1}{2}} \log(\bar{C}^{-\frac{1}{2}} C_i \bar{C}^{-\frac{1}{2}}) \bar{C}^{\frac{1}{2}} \quad (4)$$

$$\text{Exp}_{\bar{C}}(S_i) = \bar{C}^{\frac{1}{2}} \exp(\bar{C}^{-\frac{1}{2}} S_i \bar{C}^{-\frac{1}{2}}) \bar{C}^{\frac{1}{2}} \quad (5)$$

To transport points  $S_i \in \mathcal{T}_{\bar{C}} \mathcal{S}_D^+$  from the tangent space at  $\bar{C}$  to the tangent space at  $\bar{C}_\phi$ , parallel transport on  $\mathcal{S}_D^+$  can be used as:

$$\Gamma_{\bar{C} \rightarrow \bar{C}_\phi}(S_i) = P^\top S_i P, \quad P = (\bar{C}^{-1} \bar{C}_\phi)^{\frac{1}{2}} \quad (6)$$

While parallel transport is generally defined for tangent space vectors (Absil et al., 2008), for  $(\mathcal{S}_D^+, g_C^{\text{AIRM}})$  it can be directly applied without explicitly computing tangent space projections (i.e.,  $\text{Exp}_{\bar{C}_\phi} \circ \Gamma_{\bar{C} \rightarrow \bar{C}_\phi} \circ \text{Log}_{\bar{C}} = \Gamma_{\bar{C} \rightarrow \bar{C}_\phi}$ ) (Brooks et al., 2019; Yair et al., 2019).

If  $\bar{C}_\phi$  lies along the geodesic connecting  $\bar{C}$  with the identity matrix  $I_D$ , there exists a step-size  $t \in \mathbb{R}$  so that  $\bar{C}_\phi = \bar{C} \#_t I_D$ , and (6) simplifies to Mellot et al. (2024):

$$\Gamma_{\bar{C} \rightarrow I_D}(C_i; t) = \Gamma_{\bar{C} \rightarrow \bar{C} \#_t I_D}(C_i) = \bar{C}^{-\frac{t}{2}} C_i \bar{C}^{-\frac{t}{2}} \quad (7)$$

### 3 METHODS

#### 3.1 GENERATIVE MODEL

In the case of EEG, the features  $x_i \in \mathcal{X} \subseteq \mathbb{R}^{P \times T}$  comprise epochs of multivariate time-series data with  $P$  spatial channels and  $T$  consecutive temporal samples. Propagation of brain activity to the EEG electrodes, located at the scalp, is typically modeled as a linear mixture of sources (Nunez & Srinivasan, 2006):

$$x_i = A_{j(i)} z_i \quad (8)$$

where  $A_{j(i)} \in \{A \in \mathbb{R}^{P \times P} : \text{rank}(A)=P\}$  is a domain-specific forward model and  $z_i \in \mathbb{R}^{P \times T}$  the activity of latent sources. Utilizing the uniqueness of the polar decomposition for invertible matrices, we constrain the model to

$$A_j = Q \exp(P_j) \quad (9)$$

where  $Q \in \{Q \in \mathbb{R}^{P \times P} : Q^T Q = I_P\}$  is a orthogonal matrix modeling rotations and  $\exp(P_j) \in \mathcal{S}_P^+$  a SPD matrix modeling domain-specific scalings.

Like (Sabbagh et al., 2020; Kobler et al., 2021; Mellot et al., 2024), we consider zero-mean (i.e.,  $\mathbb{E}\{z_i\} = 0_P \forall i$ ) signals, and a log-linear relationship between the spatial covariance  $E_i = \text{Cov}(z_i) \in \mathcal{S}_P^+$  of the latent sources  $z_i$  and the target  $y_i$ . Specifically, we model the source covariance matrices as:

$$\log(E_i) = S_i, \quad \text{upper}(S_i) = s_i \quad (10)$$

where the invertible mapping  $\text{upper}(S) \in \mathbb{R}^{P(P+1)/2}$  extracts the upper triangular elements of a symmetric matrix while preserving its norm (i.e.,  $\|\text{upper}(S)\|_2 = \|S\|_F$ ), and latent log-space features  $s_i \in \mathbb{R}^{P(P+1)/2}$  are generated as:

$$s_i = B \tilde{y}_i + \varepsilon_i \quad (11)$$

where  $B \in \{B \in \mathbb{R}^{P(P+1)/2 \times |\mathcal{Y}|} : \text{rank}(B)=|\mathcal{Y}|\}$ ,  $\tilde{y}_i = [\delta(y_i, k) - p_j(y=y_k)]_{k=1, \dots, |\mathcal{Y}|}$  represents one-hot-coded, zero-mean labels, and  $\varepsilon_i \in \mathbb{R}^{P(P+1)/2}$  zero-mean additive noise.

**Proposition 1** *Given the specified generative model and a set of examples  $\mathcal{E}_j = \{(E_i, y_i, j) | E_i \in \mathcal{S}_P^+, y_i \in \mathcal{Y}\}_{i \leq M_j}$  of domain  $j \in \mathcal{J}$ , we have that the Fréchet mean of  $\mathcal{E}_j$ , defined in (2), converges to the identity matrix  $I_P$  with  $M_j \rightarrow \infty$  for all domains  $j \in \mathcal{J}$ .*

Our proof, provided in appendix A.1, relies on the uniqueness of the Fréchet mean for  $(\mathcal{S}_P^+, g^{\text{AIRM}})$  and that  $\tilde{y}_i$  and  $\varepsilon_i$  in (11) are zero-mean.

For the generated multi-variate time-series features  $x_i \in \mathcal{X}$  the empirical covariance matrix  $C_i$  is:

$$C_i := \text{Cov}(x_i) = \frac{1}{T} x_i x_i^T \in \mathcal{S}_P^+ \quad (12)$$

Due to the linear relationship between observed features and latent sources (8), we obtain a direct relationship to the latent source covariance matrices  $E_i$ :

$$C_i = A_{j(i)} E_i A_{j(i)}^T \quad (13)$$

Since  $E_i$  encodes the target  $y_i \in \mathcal{Y}$  and  $A_j$  is invertible,  $C_i$  are sufficient descriptors to decode  $y_i$ .

**Remark 1** *Note that for each domain  $j$  the covariance matrices of the generated data  $\{C_i : j_i = j\}$  are not necessarily jointly diagonalizable. Depending on the structure of  $B$  and  $\varepsilon_i$ , the proposed generative model reduces to a jointly diagonalizable model if all the off-diagonal elements in  $\log(E_i)$  are zero  $\forall i$ .*

#### 3.2 DECODING FRAMEWORK

Given source domain data  $\mathcal{D}_s$  and a hypothesis class  $\mathcal{H}$ , we aim to learn a decoder function  $h_s \in \mathcal{H}$ , and - once the unlabeled target data  $\mathcal{D}_t$  is revealed - use  $\mathcal{D}_t$  and  $h_s$  to learn  $h_t \in \mathcal{H}$ . Following (Kobler et al., 2022a), we constrain the hypothesis class  $\mathcal{H}$  to functions  $h : \mathcal{X} \times \mathcal{J} \rightarrow \mathcal{Y}$  that can be decomposed into a composition of a shared feature extractor  $f_\theta : \mathcal{X} \rightarrow \mathcal{S}_D^+$  (Figure 1b), latent alignment  $m_\phi : \mathcal{S}_D^+ \times \mathcal{J} \rightarrow \mathbb{R}^{D(D+1)/2}$  (Figure 1c), and a shared linear classifier  $g_\psi : \mathbb{R}^{D(D+1)/2} \rightarrow \mathcal{Y}$  (Figure 1d) with parameters  $\Theta = \{\theta, \phi, \psi\}$ . Within this section, we focus on theoretical considerations for  $m_\phi$  under our generative model.

**Tangent space mapping (TSM) to recover  $\log(E_i)$**  Considering a set of labeled data  $\mathcal{D} = \{(x_i, y_i) : x_i \in \mathcal{X}, y_i \in \mathcal{Y}, j_i=j \forall i\}$  obtained from a single domain  $j$ , TSM (Barachant et al., 2011) provides an established (Lotte et al., 2018; Jayaram & Barachant, 2018) decoding approach to infer  $y_i$ . TSM requires SPD-matrix valued representations. For the considered generative model, covariance features  $C_i$ , as defined in (5), are a natural choice (i.e.,  $f_\theta \triangleq \text{Cov}$ ). In a nutshell, TSM first estimates the Fréchet mean  $\bar{C}$  of  $\mathcal{C} = \{\text{Cov}(x_i) : (x_i, y_i) \in \mathcal{D}\}$ , projects each  $C_i$  to the tangent space at  $\bar{C}$ , and finally transports the data to vary around  $I_P$ . Formally,

$$\tilde{m}_\phi(C_i) := \text{upper} \circ \Gamma_{\bar{C} \rightarrow I} \circ \text{Log}_{\bar{C}}(C_i) = \text{upper} \left( \log \left( \bar{C}^{-\frac{1}{2}} C_i \bar{C}^{-\frac{1}{2}} \right) \right), \phi = \{\bar{C}\} \quad (14)$$

where the resulting representations  $\tilde{m}_\phi(C_i) \in \mathbb{R}^{P(P+1)/2}$  have a linear relationship to  $\log(E_i)$  (Sabbagh et al., 2020; Kobler et al., 2021) and through (10) and (11) also to the labels  $y_i$ .

**RCT+TSM compensates marginal and conditional shifts** In the context of functional neuroimaging data, the recentering (RCT) transform (Zanini et al., 2017; Yair et al., 2019) and its extensions (Rodrigues et al., 2019; He & Wu, 2019; Kobler et al., 2022a; Mellot et al., 2023) address source-free UDA problems. Combined with TSM, RCT+TSM essentially applies (14) independently to each domain  $j$ . The outputs  $\tilde{m}_{\phi(j(i))}(C_i)$ , where  $\phi(j) = \{\bar{C}_j\}$ , are treated as domain-invariant and passed on to the shared classifier  $g_\psi : \mathbb{R}^{D(D+1)/2} \rightarrow \mathcal{Y}$ .

Although RCT+TSM is an established method to address SFUDA problems for neuroimaging data (Lotte et al., 2018; Wei et al., 2022; Roy et al., 2022), there is a lack of understanding of what kind of distribution shifts RCT+TSM can compensate.

**Proposition 2** *For the generative model, specified in section 3.1, RCT+TSM compensates conditional distribution shifts introduced by the invertible linear map  $A_j$ , defined in (8), and recovers domain-invariant representations if there are no label shifts (i.e.,  $p_j(y=y) = p(y=y) \forall y \in \mathcal{Y}, \forall j \in \mathcal{J}_s \cup \mathcal{J}_t$ ).*

A detailed proof is provided in appendix A.2. Starting with  $\tilde{m}_{\phi(j(i))}(C_i)$ , as defined in (14) and utilizing the unique polar decomposition (9) of  $A_j$  into rotational  $Q$  and scaling  $\exp(P_j)$  transformations along with proposition 1 we obtain:

$$\log \left( \bar{C}_{j(i)}^{-\frac{1}{2}} C_i \bar{C}_{j(i)}^{-\frac{1}{2}} \right) = Q \log(E_i) Q^T = Q \text{upper}^{-1} \left( B \left( 1_{y_i} - \bar{y}_{j(i)} \right) + \varepsilon_i \right) Q^T \quad (15)$$

where the vector  $\bar{y}_j = [p_j(y=y)]_{y=1, \dots, |\mathcal{Y}|}$  contains the class priors for domain  $j$ . If there are no label shifts the class priors are constant  $p_j(y=y) = p(y=y) \forall y \in \mathcal{Y}, \forall j \in \mathcal{J}_s \cup \mathcal{J}_t \implies \bar{y}_j = \bar{y}$ , and (15) only contains domain-invariant terms on the right hand side. Thus, RCT+TSM compensates the conditional shifts introduced by  $\exp(P_j)$ .  $\square$

**Remark 2** *If all sources in (8) can be partitioned into relevant and irrelevant sources  $z_i = [z_i^\parallel, z_i^\perp]$ ,  $z_i^\parallel = f(y_i)$ ,  $z_i^\perp \neq f(y_i)$  that are independent from each other, the source covariance matrices  $E_i$  have a block-diagonal structure. Then, RCT+TSM compensates marginal shifts in  $z_i^\perp$  and conditional shifts in  $z_i^\parallel$  introduced by  $\exp(P_j)$ .*

**Alignment under label shifts** We aim to extend RCT+TSM to extract label shift invariant representations. Specifically, we aim to apply additional transformations on  $(\mathcal{S}_D^+, g^{\text{AIRM}})$  that attenuate the effect of class priors  $\bar{y}_j$  in (15). We first rewrite (15) as:

$$\bar{C}_{j(i)}^{-\frac{1}{2}} C_i \bar{C}_{j(i)}^{-\frac{1}{2}} = \exp(Q \log(E_i) Q^T) = \exp(Q \text{upper}^{-1} \left( B \left( 1_{y_i} - \bar{y}_{j(i)} \right) + \varepsilon_i \right) Q^T) \quad (16)$$

$$= \exp \left( Q \underbrace{\text{upper}^{-1} \left( B 1_{y_i} + \varepsilon_i \right) Q^T}_{\log(\tilde{E}_i)} - Q \underbrace{\text{upper}^{-1} \left( B \bar{y}_{j(i)} \right) Q^T}_{\tilde{P}_{j(i)}} \right) \quad (17)$$

where we split  $\log(E_i)$  into domain-invariant  $\log(\tilde{E}_i)$  and label shift  $\tilde{P}_{j(i)}$  terms. To separate both terms into products of matrices, we utilize  $\exp(\alpha(A + B)) = \exp(\alpha B/2) \exp(\alpha A) \exp(\alpha B/2) +$

$\mathcal{O}(\alpha^3)$  (Higham, 2008, Theorem 10.5), resulting in:

$$\bar{C}_{j(i)}^{-\frac{1}{2}} C_i \bar{C}_{j(i)}^{-\frac{1}{2}} = Q \exp(\bar{P}_{j(i)})^{-\frac{1}{2}} Q^T Q \tilde{E}_i Q^T Q \exp(\bar{P}_{j(i)})^{-\frac{1}{2}} Q^T + \mathcal{O}(\|\log(E_i)\|_F^3) \quad (18)$$

with the approximation error  $\mathcal{O}(\|\log(E_i)\|_F^3)$  decaying cubically for  $\|\log(E_i)\|_F < 1$ . In this form, it is straightforward to see that an additional bilinear transformation on the left hand side in (18) with an SPD matrix can approximately compensate the effect of  $\exp(\bar{P}_{j(i)})$ . We denote this parameter as domain-specific bias parameter  $\Phi_{j(i)} \in \mathcal{S}_D^+$ , and generalize RCT+TSM to:

$$m_{\phi(j(i))}(C_i) = \text{upper} \circ \log \left( \Phi_{j(i)}^{\frac{1}{2}} \bar{C}_{j(i)}^{-\frac{1}{2}} C_i \bar{C}_{j(i)}^{-\frac{1}{2}} \Phi_{j(i)}^{\frac{1}{2}} \right), \quad \phi(j(i)) = \{\bar{C}_{j(i)}, \Phi_{j(i)}\} \quad (19)$$

Note that if  $\exp(\bar{P}_j)$  and  $\exp(P_j)$  share the same eigenvectors, they commute and lie on the same geodesic connecting  $\exp(P_j)$  with  $I_D$ . Consequently, the combined effect of  $\exp(\bar{P}_j)$  and  $\exp(P_j)$  is constrained to the geodesic connecting  $\bar{C}_j$  with  $I_D$ . Then, the solution space can be constrained to  $\Phi_j \in \{\Phi : \Phi \in \mathcal{S}_D^+, \Phi = \bar{C}_j \#_{\varphi_j} I_D, \varphi_j \in \mathbb{R}\}$ , and (7) used to simplify (19) to:

$$m_{\phi(j(i))}(C_i) = \text{upper} \circ \log \circ \Gamma_{\bar{C}_{j(i)} \rightarrow \bar{C}_{j(i)} \#_{\varphi_{j(i)}} I_D}(C_i), \quad \phi(j(i)) = \{\bar{C}_{j(i)}, \varphi_{j(i)}\} \quad (20)$$

where the geodesic step-size parameter  $\varphi_{j(i)} \in \mathbb{R}$  needs to be learned.

**Latent alignment with domain-specific SPD batch norm.** Parametrizing the feature extractor  $f_\theta : \mathcal{X} \rightarrow \mathcal{S}_P^+$  as a neural network naturally extends the decoding framework to neural networks with SPD matrix-valued features (Huang & Gool, 2017). In this end-to-end learning setting, SPD batch norm (SPDBN)(Brooks et al., 2019; Kobler et al., 2022b) and domain-specific batch norm (Kobler et al., 2022a) layers can be utilized to implement  $m_\phi$ .

### 3.3 SPD MANIFOLD INFORMATION MAXIMIZATION

We utilize the labeled source domain dataset  $\mathcal{D}_s$  to learn the shared feature extractor  $f_\theta, g_\psi$ , as well as  $m_\phi$  for the source domains  $j \in \mathcal{J}_s$ . Specifically, we used the cross-entropy loss as the training objective, employing the PyTorch framework (Paszke et al., 2019) with extensions for structured matrices (Ionescu et al., 2015) and manifold-constrained gradients (Absil et al., 2008) to propagate gradients through the layers. Gradients were estimated using fixed-size mini-batches (50 observations; 10 per domain across 5 domains) and updated parameters with the Riemannian ADAM optimizer (Béćigneul & Ganea, 2018) (10<sup>-3</sup> learning rate, 10<sup>-4</sup> weight decay,  $\beta_1 = 0.9$ ,  $\beta_2 = 0.999$ ). We split the source domains' data into training and validation sets (80% / 20% splits, randomized, stratified by domain and label) and iterated through the training set for 100 epochs using exhaustive minibatch sampling.

For the target domains, we keep  $f_\theta$  and  $g_\psi$  fixed and learn  $\phi(j) \forall j \in \mathcal{J}_t$ . Specifically, for each domain  $j \in \mathcal{J}_t$ , we use (2) to compute the Fréchet mean  $\bar{C}_{j(i)}$  of  $\mathcal{C}_j = \{f_\theta(x_i) : (x_i, j(i)) \in \mathcal{D}_t, j(i) = j\}$ . To estimate  $\Phi_{j(i)}$  in an unsupervised fashion, we propose SPD manifold information maximization (SPDIM). SPDIM employs the information maximization (IM) loss (Shi & Sha, 2012) to ensure that target outputs are individually certain and globally diverse. The IM loss is a popular training objective for SFUDA and test-time adaptation frameworks (Liang et al., 2020; 2024).

Depending on the choice of bias parameter, we distinguish between SPDIM(bias) defined in (19) and SPDIM(geodesic) defined in equation (20). In practice, when the target domain data is revealed, we initialize  $\Phi_{j(i)}$  with  $I_D$  and  $\varphi_{j(i)}$  with 1. We then minimize the following  $\mathcal{L}_{\text{CEM}}$  and  $\mathcal{L}_{\text{MEM}}$  that together constitute the  $\mathcal{L}_{\text{IM}}$  loss:

$$\mathcal{L}_{\text{IM}} = \mathcal{L}_{\text{CEM}} + \mathcal{L}_{\text{MEM}} \quad (21)$$

$$\mathcal{L}_{\text{CEM}} = -\mathbb{E}_{(x_i, j_i) \in \mathcal{D}_t} \left\{ \sum_{k=1}^{|\mathcal{Y}|} \delta_k \left( \frac{h_t(x_i, j_i)}{T} \right) \log \delta_k \left( \frac{h_t(x_i, j_i)}{T} \right) \right\}$$

$$\mathcal{L}_{\text{MEM}} = \sum_{k=1}^{|\mathcal{Y}|} \hat{p}_k \log \hat{p}_k, \quad \hat{p}_k = \mathbb{E}_{(x_i, j_i) \in \mathcal{D}_t} \left\{ \delta_k \left( \frac{h_t(x_i, j_i)}{T} \right) \right\}$$

where  $\delta_k$  is the  $k$ -th element of the softmax output,  $\mathcal{L}_{\text{CEM}}$  is conditional entropy minimization,  $\mathcal{L}_{\text{MEM}}$  is marginal entropy maximization and factor  $T$  is temperature scaling. IM balance is more effective than conditional entropy minimization because minimizing only the conditional entropy may lead to mode collapse with all test data allocated to one class (Grandvalet & Bengio, 2004). We additionally employed a temperature scaling factor  $T$  to adjust the model's prediction confidence on the target data, a common technique for calibrating probabilistic models (Li et al., 2023; Guo et al., 2017). Temperature scaling uses a single scalar parameter  $T > 0$  for all classes, and it increases the softmax output entropy when  $T > 1$  and decreases it when  $0 < T < 1$ .

## 4 EXPERIMENTS

We conducted simulations and experiments with public EEG motor imagery and sleep stage datasets to evaluate our proposed framework empirically. We followed Kobler et al. (2022a) to fit the source decoder  $h_s$ . Then, we use  $h_s$  together with  $\mathcal{D}_t$  to evaluate SPDIM(bias) against SPDIM(geodesic) and other baseline SFUDA methods, categorized as:

**Recentering** (RCT) As discussed in section 3.2, this baseline transports the latent covariance features from their domain-specific Fréchet mean to the identity matrix.

**Information maximization** (IM) Similar to Li et al. (2023), this method minimizes the  $\mathcal{L}_{\text{IM}}$  loss in (21) to fine-tune all model parameters (i.e., IM(all)),  $g_\psi$  (i.e., IM(classifier)) or merely the bias parameter of  $g_\psi$  (i.e., IM(classifier bias)).

**No domain adaptation** (w/o) Methods in this category treat the problem as a standard supervised learning problem; they do not utilize the domain labels  $\mathcal{J}_s \cup \mathcal{J}_t$  during training and testing. In models that perform TSM, all data are projected to the tangent space at the Fréchet mean of the source domain data.

We used publicly available Python code for baseline methods and implemented custom methods using the packages torch (Paszke et al., 2019), scikit-learn (Pedregosa et al., 2011), braindecode (Schirrmeister et al., 2017), geoopt (Kochurov et al., 2020) and pyRiemann Barachant et al. (2023). We conducted the experiments on standard computation PCs with 32-core CPUs, 128 GB of RAM, and a single GPU.

### 4.1 SIMULATIONS

To examine the effectiveness of SPDIM, we simulated binary classification problems under our generative model. We directly generated  $2 \times 2$  covariance matrices  $C_i$ . To do so, we first generated log-space features  $s_i \in \mathbb{R}^3$ , defined in (11), using the scikit-learn function `make_classification` with 1 encoding source, 2 noise sources, and varied the class separability parameter to simulate different signal-to-noise ratios. The data were then normalized to have zero mean and unit variance. To obtain  $E_i \in \mathcal{S}_D^+$ , we applied  $\text{upper}^{-1}$  and  $\text{Exp}_{I_D}$ , as defined in (5). At this level, the data were split into source domain and target domain data, with each domain containing 250 observations per class. Finally, the data were projected to the channel space using domain-specific mixing matrices  $A_j$ , as defined in (9). To vary the degree of label shift, we artificially varied the label ratio, defined as the proportion of the minority class to the majority class, in the target domain via randomly dropping samples. We used balanced accuracy as the evaluation metric and examined the performance of each method with different class separability under different imbalance ratios.

The results are summarized in Figure 2. The simulation results demonstrate that as the label shifts become more severe (i.e., lower label ratio), all methods suffer from performance decreases. Still, SPDIM (bias) outperforms the considered baseline approaches in maintaining a higher score for the same label ratio and signal-to-noise ratio (i.e., class separability). Even in severe cases (0.1 label ratio), SPDIM (bias) improves upon RCT by more than 5% for moderate to high signal-to-noise ratios. Figure 1 b-d visualizes the representations obtained with RCT (top) and SPDIM (bottom) for a representative example.

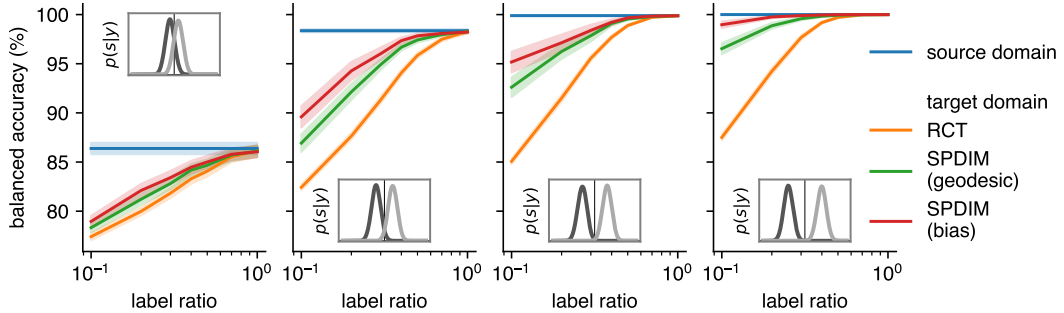


Figure 2: **SPDIM simulation results** for 2 classes,  $2 \times 2$  covariance features and 1 source and 1 target domain. Balanced accuracy scores (higher is better) across target domain label ratios (majority to minority class) on the x-axis and class separability  $p(s|y)$  across panels. Source domain labels were balanced.

#### 4.2 EEG MOTOR IMAGERY DATA

We considered 4 public motor imagery datasets: BNCI2014001 (Tangermann et al., 2012) (9 subjects/2 sessions/4 classes/22 channels), BNCI2015001 (Faller et al., 2012) (12/2-3/2/13), Zhou2016 (Zhou et al., 2016) (4/3/3/14), and BNCI2014004 (Leeb et al., 2007) (9/5/2/3). We used MOABB (Jayaram & Barachant, 2018; Chevallier et al., 2024) to pre-process the continuous time-series data and extract labeled epochs. Pre-processing included resampling EEG signals to 250 or 256 Hz, applying temporal filters to capture frequencies between 4 and 36 Hz, and extracting 3-second epochs linked to specific class labels. Following Kobler et al. (2022a), we use TSMNet as the model and treat sessions as domains, and use a leave-one-group-out cross-validation (CV) scheme to fit and evaluate the methods. To evaluate cross-session transfer, we fitted and evaluated models independently per subject and treated the session as the grouping variable. To evaluate cross-subject transfer, we treated the subject as the grouping variable. After running pilot experiments with the BNCI2014001 dataset, we set the temperature scaling factor in (21) to  $T = 2$  for binary classification problems and  $T = 0.8$  otherwise. Other hyper-parameters (e.g., early stopping) were fit with a single stratified (domain and labels) inner train/validation split. As in the simulation experiment, we artificially introduced label shifts in the target domains. We used balanced accuracy as the metric to examine the performance of each method at label ratios of 1.0 and 0.2 for the source and target domains, respectively.

Grand average results across all 4 datasets are summarized in Figure 3, and grouped by the transfer learning scenario (cross-session, cross-subject). To attenuate large variability across subjects, we report scores relative to the score obtained with RCT w/o label shifts (i.e., 1.0 label ratio). Although no method can perfectly compensate the artificially introduced label shifts, SPDIM(bias) is consistently at the top (cross-subject) or among the top (cross-session) performing methods. Significance testing ( $n=34$  subjects), summarized in Supplementary Table A3, revealed that performance for SPDIM(bias) is significantly higher than w/o, RCT, IM(classifier), and IM(all) in the cross-subject setting as well as RCT, IM(classifier), and IM(all) in the cross-session scenario.

#### 4.3 EEG-BASED SLEEP STAGING

The aim of this experiment is to demonstrate the effectiveness of our method on datasets with inherent label shifts. Due to the inherent variability of sleep, most sleep stage datasets exhibit label shifts across subjects (Eldele et al., 2023). Sleep stage classification plays a key role in assessing sleep quality and diagnosing sleep disorders (Perez-Pozuelo et al., 2020). Yet, automated frameworks lack accuracy and suffer from poor generalization across domains, resulting in accuracy drops compared to expert neurologists.

We considered 4 public sleep stage datasets: CAP (Terzano et al., 2001; Goldberger et al., 2000), Dreem (Guillot et al., 2020), HMC (Alvarez-Estevez & Rijsman, 2021a;b), and ISRUC (Khalighi et al., 2016). A detailed description is provided in Supplementary Table A1. We consider sleep stages following the AASM (Berry et al., 2012) standard (W, N1, N2, N3, REM). If data was orig-

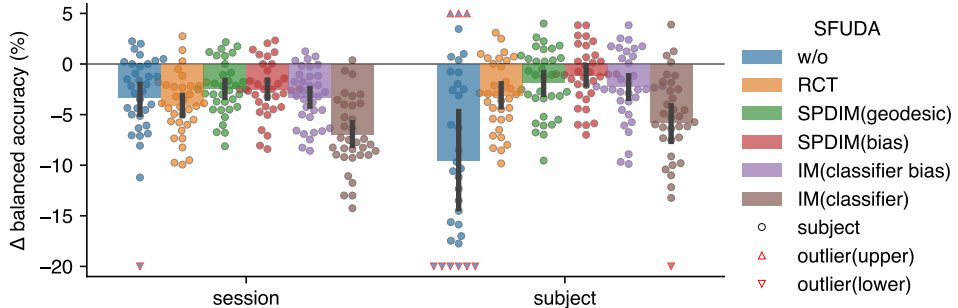


Figure 3: **Motor-imagery results (0.2 label ratio).** Average of test-set scores (balanced accuracy; higher is better; standard-deviation in brackets) relative to TSMNet+RCT (Kobler et al., 2022a) applied to balanced target domain data (i.e., 1.0 imbalance ratio). For extended results per dataset, see Supplementary Table A3.

inally scored following the K&M (Wolpert, 1969) standard (W, S1, S2, S3, S4, REM), we merged stages S3 and S4 into a single stage N3. EEG data pre-processing followed (Guillot & Thorey, 2021) and was implemented with MNE-python (Gramfort et al., 2014). First, all EEG channels were retained, and an IIR band-pass filter ranging from 0.2 to 30 Hz was applied. The signals were then resampled to 100 Hz, and non-overlapping 30-second epochs were extracted together with the associated labels. To attenuate the effects of gross outliers, each recording was scaled to have unit inter-quartile range and a median of zero, and values exceeding 20 times the inter-quartile range were clipped Perslev et al. (2021). Lastly, subjects with corrupted data (e.g., mismatched labels and epochs) were excluded, resulting in a total of 426 remaining subjects.

Since label shifts occur in the source domains of sleep stage data, the considered models are trained with a balanced mini-batch sampler, which is a popular method to compensate for label shifts during training in deep learning (Cao et al., 2019). The balanced sampler over-sampled minority classes to ensure that the label distribution per domain is balanced within each mini-batch.

To evaluate the methods, we employed a 10-fold grouped cross-validation scheme, ensuring that each group (i.e., subject) appears either in the training set (i.e., source domains) or the test set (i.e., target domains). As before, we set the temperature scaling factor  $T = 0.8$  and used stratified (labels and domains) inner train/validation splits for early stopping. In addition to the baseline methods introduced before, we included two additional benchmark deep learning architectures that were specifically proposed for sleep staging: Chambon (Chambon et al., 2018) and Usleep (Perslev et al., 2021). For both architectures, we use the implementation provided in braindecode (Schirrmeister et al., 2017).

Table 1 summarizes the results across datasets along with the grand average results of published baseline methods. Extended results for all considered baseline methods are listed in Supplementary Table A2. Interestingly, TSMNet+RCT (Kobler et al., 2022a) obtained similar or higher results compared to non-SFUDA baselines. TSMNet+SPDIM(bias) significantly outperforms all other methods for the patient and healthy subject groups. Overall, the margin to TSMNet+RCT was approx. 5% in the patient group, which indicates that our proposed method has great potential for clinical applications.

**Ablation Study** Table 2 summarizes grand average test scores relative to SPDIM(bias). We highlight three observations. First, all considered ablations lead to a significant performance drop of at least 3% compared to SPDIM(bias), suggesting the combined importance of IM paired with the manifold-constrained bias parameter and RCT. Second, fine-tuning the classifier bias parameter yields approximately the same performance as SPDIM(geodesic), extending the finding of (Mellot et al., 2024) from regression to classification scenarios. Third, IM SFUDA methods obtained the top 3 scores, but two variants (IM(classifier) and IM(full)) failed to improve upon the non-SFUDA method, which underscores the importance of selecting the right parameter to prevent the IM loss from over-fitting.

Model	Dataset: SFUDA	CAP		Dreem		HMC		ISRUC		Overall	
		patient (n=82)	healthy (n=22)	patient (n=50)	patient (n=154)	healthy (n=10)	patient (n=108)	healthy (n=32)	patient (n=394)	healthy (n=32)	patient (n=394)
Chambon	w/o	• 64.7 (10.7)	• 65.2 (9.1)	• 53.4 (16.2)	• 64.0 (9.6)	72.7 (3.9)	• 68.9 (8.2)	• 67.5 (8.6)	• 64.2 (11.5)		
USleep	w/o	• 59.1 (10.3)	• 55.9 (8.3)	• 48.4 (8.2)	• 66.6 (9.3)	72.9 (6.1)	• 68.8 (8.3)	• 61.3 (11.0)	• 63.3 (11.3)		
TSMNet	w/o	• 68.0 (11.2)	• 65.9 (9.6)	66.7 (12.4)	• 63.6 (11.3)	73.4 (3.9)	• 68.7 (9.3)	• 68.3 (8.9)	• 66.3 (11.1)		
	RCT	• 68.2 (8.8)	• 68.9 (5.8)	• 64.2 (8.5)	• 62.2 (6.0)	• 72.8 (2.8)	• 66.6 (6.4)	• 70.1 (5.3)	• 64.9 (7.5)		
	SPDIM (bias) (proposed)	<b>71.0</b> (9.6)	<b>72.1</b> (8.0)	<b>68.1</b> (9.8)	<b>68.6</b> (8.5)	<b>76.7</b> (3.4)	<b>71.6</b> (6.9)	<b>73.5</b> (7.2)	<b>69.9</b> (8.6)		

Table 1: **Sleep-staging results per dataset.** Average of test-set scores (balanced accuracy; higher is better; standard-deviation in brackets). Permutation-paired t-tests were used to identify significant differences between TSMNet+SPDIM (*proposed*) and baseline methods (1e4 permutations, 4 tests, t-max correction). Significant differences are highlighted (•  $p \leq 0.05$ , •  $p \leq 0.01$ , •  $p \leq 0.001$ ). Extended results are provided in Supplementary Table A2.

SFUDA	$\Delta$ balanced accuracy (%)	
	mean (std)	t-val (p-val)
SPDIM(bias)	-	-
SPDIM(geodesic)	-3.0 (3.6)	-17.4 (0.0001)
RCT	-4.8 (4.5)	-22.1 (0.0001)
w/o	-3.7 (8.5)	-9.0 (0.0001)
IM(classifier bias)	-3.0 (3.8)	-16.1 (0.0001)
IM(classifier)	-4.8 (5.4)	-18.5 (0.0001)
IM(all)	-27.1 (13.5)	-41.5 (0.0001)

Table 2: **Sleep-staging ablation results.** Balanced accuracy scores (higher is better) relative to the proposed method for the combined sleep staging data. Averages and standard deviation summarize the individual (n=426 subjects) test-set scores. Student’s t values and adjusted p values indicate the effect strength (permutation-paired t-tests, 1e4 permutations, 6 tests, t-max correction).

## 5 DISCUSSION

We proposed a geometric deep learning framework, denoted SPDIM, to address SFUDA problems with conditional and label shifts and demonstrated its utility in highly relevant EEG-based neurotechnology application scenarios. We first introduced a realistic generative model, and provided theoretical analyses showing that prior Riemannian statistical alignment methods that align the Fréchet mean can compensate for the conditional distribution shifts introduced in our generative model, but hurt generalization under additional label shifts. As a remedy, we proposed SPDIM to learn a domain-specific SPD manifold-constrained bias parameter to compensate over-corrections introduced via aligning the Fréchet means by employing the information maximization principle. In simulations and experiments with real EEG data, SPDIM consistently achieved the highest scores among the considered baseline methods.

## 6 ACKNOWLEDGMENTS

Motoaki Kawanabe and Reinmar J Kobler were partially supported by the Innovative Science and Technology Initiative for Security Grant Number JPJ004596, ATLA, Japan.

## 7 AUTHOR CONTRIBUTIONS

Shanglin Li contributed to the study under the co-supervision of Motoaki Kawanabe and Reinmar J. Kobler. Shanglin Li and Reinmar J. Kobler developed the decoding methods. Reinmar J. Kobler contributed the theoretical analysis. Shanglin Li and Reinmar J. Kobler performed the simulation experiments. Shanglin Li conducted the experiments with EEG data. The draft of the manuscript was written by Shanglin Li and Reinmar Kobler. All authors read and approved the final manuscript.

## REFERENCES

P-A Absil, Robert Mahony, and Rodolphe Sepulchre. *Optimization algorithms on matrix manifolds*. Princeton University Press, 2008.

Turkey N Alotaiby, Saleh A Alshebeili, Tariq Alshawi, Ishtiaq Ahmad, and Fathi E Abd El-Samie. Eeg seizure detection and prediction algorithms: a survey. *EURASIP Journal on Advances in Signal Processing*, 2014:1–21, 2014. doi: 10.1186/1687-6180-2014-183.

Diego Alvarez-Estevez and RM Rijssman. Haaglanden medisch centrum sleep staging database (version 1.0. 1). *PhysioNet*, 2021a. doi: 10.13026/t79q-fr32.

Diego Alvarez-Estevez and Roselyne M Rijssman. Inter-database validation of a deep learning approach for automatic sleep scoring. *PloS one*, 16(8):e0256111, 2021b. doi: 10.1371/journal.pone.0256111.

Stylianos Bakas, Siegfried Ludwig, Dimitrios A Adamos, Nikolaos Laskaris, Yannis Panagakis, and Stefanos Zafeiriou. Latent alignment with deep set eeg decoders. *arXiv preprint arXiv:2311.17968*, 2023.

Alexandre Barachant, Stéphane Bonnet, Marco Congedo, and Christian Jutten. Multiclass brain–computer interface classification by riemannian geometry. *IEEE Transactions on Biomedical Engineering*, 59(4):920–928, 2011. doi: 10.1109/TBME.2011.2172210.

Alexandre Barachant, Quentin Barthélémy, Jean-Rémi King, Alexandre Gramfort, Sylvain Chevalier, Pedro L. C. Rodrigues, Emanuele Olivetti, Vladislav Goncharenko, Gabriel Wagner vom Berg, Ghiles Reguig, Arthur Lebeurrier, Erik Bjäreholt, Maria Sayu Yamamoto, Pierre Clisson, and Marie-Constance Corsi. pyriemann/pyriemann: v0.5, 2023. URL <https://doi.org/10.5281/zenodo.8059038>.

Gary Bécigneul and Octavian-Eugen Ganea. Riemannian adaptive optimization methods. *arXiv preprint arXiv:1810.00760*, 2018.

Shai Ben-David, John Blitzer, Koby Crammer, Alex Kulesza, Fernando Pereira, and Jennifer Wortman Vaughan. A theory of learning from different domains. *Machine learning*, 79:151–175, 2010. doi: 10.1007/s10994-009-5152-4.

Richard B Berry, Rohit Budhiraja, Daniel J Gottlieb, David Gozal, Conrad Iber, Vishesh K Kapur, Carole L Marcus, Reena Mehra, Sairam Parthasarathy, Stuart F Quan, et al. Rules for scoring respiratory events in sleep: update of the 2007 aasm manual for the scoring of sleep and associated events: deliberations of the sleep apnea definitions task force of the american academy of sleep medicine. *Journal of clinical sleep medicine*, 8(5):597–619, 2012. doi: 10.5664/jcsm.2172.

Rajendra Bhatia. *Positive definite matrices*. Princeton university press, 2009. ISBN 978-0-691-12918-1.

Rajendra Bhatia. The Riemannian Mean of Positive Matrices. In Frank Nielsen and Rajendra Bhatia (eds.), *Matrix Information Geometry*, pp. 35–51. Springer Berlin Heidelberg, Berlin, Heidelberg, 2013. ISBN 978-3-642-30232-9. doi: 10.1007/978-3-642-30232-9\_2.

Daniel Brooks, Olivier Schwander, Frédéric Barbaresco, Jean-Yves Schneider, and Matthieu Cord. Riemannian batch normalization for spd neural networks. *Advances in Neural Information Processing Systems*, 32, 2019.

Kaidi Cao, Colin Wei, Adrien Gaidon, Nikos Arechiga, and Tengyu Ma. Learning imbalanced datasets with label-distribution-aware margin loss. *Advances in neural information processing systems*, 32, 2019.

Stanislas Chambon, Mathieu N Galtier, Pierrick J Arnal, Gilles Wainrib, and Alexandre Gramfort. A deep learning architecture for temporal sleep stage classification using multivariate and multi-modal time series. *IEEE Transactions on Neural Systems and Rehabilitation Engineering*, 26(4):758–769, 2018. doi: 10.1109/TNSRE.2018.2813138.

Sylvain Chevallier, Igor Carrara, Bruno Aristimunha, Pierre Guetschel, Sara Sedlar, Bruna Lopes, Sébastien Velut, Salim Khazem, and Thomas Moreau. The largest EEG-based BCI reproducibility study for open science: the MOABB benchmark, April 2024. URL <http://arxiv.org/abs/2404.15319>.

Marco Congedo, Alexandre Barachant, and Rajendra Bhatia. Riemannian geometry for eeg-based brain-computer interfaces; a primer and a review. *Brain-Computer Interfaces*, 4(3):155–174, 2017. doi: 10.1080/2326263X.2017.1297192.

Emadeldeen Eldele, Mohamed Ragab, Zhenghua Chen, Min Wu, Chee-Keong Kwoh, and Xiaoli Li. Self-supervised learning for label-efficient sleep stage classification: A comprehensive evaluation. *IEEE Transactions on Neural Systems and Rehabilitation Engineering*, 31:1333–1342, 2023. doi: 10.1109/TNSRE.2023.3245285.

Stephen H Fairclough and Fabien Lotte. Grand challenges in neurotechnology and system neuroergonomics. *Frontiers in Neuroergonomics*, 1:602504, 2020. doi: 10.3389/fnrgo.2020.602504.

Josef Faller, Carmen Vidaurre, Teodoro Solis-Escalante, Christa Neuper, and Reinhold Scherer. Autocalibration and recurrent adaptation: Towards a plug and play online erd-bci. *IEEE Transactions on Neural Systems and Rehabilitation Engineering*, 20(3):313–319, 2012. doi: 10.1109/TNSRE.2012.2189584.

Ary L Goldberger, Luis AN Amaral, Leon Glass, Jeffrey M Hausdorff, Plamen Ch Ivanov, Roger G Mark, Joseph E Mietus, George B Moody, Chung-Kang Peng, and H Eugene Stanley. Physiobank, physiotoolkit, and physionet: components of a new research resource for complex physiologic signals. *circulation*, 101(23):e215–e220, 2000. doi: 10.1161/01.cir.101.23.e215.

Alexandre Gramfort, Martin Luessi, Eric Larson, Denis A Engemann, Daniel Strohmeier, Christian Brodbeck, Lauri Parkkonen, and Matti S Hämäläinen. Mne software for processing meg and eeg data. *neuroimage*, 86:446–460, 2014. doi: 10.1016/j.neuroimage.2013.10.027.

Yves Grandvalet and Yoshua Bengio. Semi-supervised learning by entropy minimization. *Advances in neural information processing systems*, 17, 2004.

Antoine Guillot and Valentin Thorey. Robustsleepnet: Transfer learning for automated sleep staging at scale. *IEEE Transactions on Neural Systems and Rehabilitation Engineering*, 29:1441–1451, 2021. doi: 10.1109/TNSRE.2021.3098968.

Antoine Guillot, Fabien Sauvet, Emmanuel H During, and Valentin Thorey. Dreem open datasets: Multi-scored sleep datasets to compare human and automated sleep staging. *IEEE transactions on neural systems and rehabilitation engineering*, 28(9):1955–1965, 2020. doi: 10.1109/TNSRE.2020.3011181.

Chuan Guo, Geoff Pleiss, Yu Sun, and Kilian Q Weinberger. On calibration of modern neural networks. In *International conference on machine learning*, pp. 1321–1330. PMLR, 2017.

He He and Dongrui Wu. Transfer learning for brain–computer interfaces: A euclidean space data alignment approach. *IEEE Transactions on Biomedical Engineering*, 67(2):399–410, 2019. doi: 10.1109/TBME.2019.2913914.

Nicholas J. Higham. *Functions of Matrices: Theory and Computation*. Society for Industrial and Applied Mathematics, January 2008. ISBN 978-0-89871-646-7 978-0-89871-777-8. doi: 10.1137/1.9780898717778. URL <http://epubs.siam.org/doi/book/10.1137/1.9780898717778>.

Judy Hoffman, Mehryar Mohri, and Ningshan Zhang. Algorithms and theory for multiple-source adaptation. *Advances in neural information processing systems*, 31, 2018.

Zhiwu Huang and Luc Van Gool. A Riemannian Network for SPD Matrix Learning. In *Proceedings of the Thirty-First AAAI Conference on Artificial Intelligence*, AAAI'17, pp. 2036–2042. AAAI Press, 2017.

Catalin Ionescu, Orestis Vantzos, and Cristian Sminchisescu. Matrix backpropagation for deep networks with structured layers. In *Proceedings of the IEEE international conference on computer vision*, pp. 2965–2973, 2015.

Vinay Jayaram and Alexandre Barachant. Moabb: trustworthy algorithm benchmarking for bcis. *Journal of neural engineering*, 15(6):066011, 2018. doi: 10.1088/1741-2552/aadea0.

Sirvan Khalighi, Teresa Sousa, José Moutinho Santos, and Urbano Nunes. Isruc-sleep: A comprehensive public dataset for sleep researchers. *Computer methods and programs in biomedicine*, 124:180–192, 2016. doi: 10.1016/j.cmpb.2015.10.013.

Reinmar Kobler, Jun-ichiro Hirayama, Qibin Zhao, and Motoaki Kawanabe. Spd domain-specific batch normalization to crack interpretable unsupervised domain adaptation in eeg. *Advances in Neural Information Processing Systems*, 35:6219–6235, 2022a.

Reinmar J Kobler, Jun-ichiro Hirayama, Lea Hehenberger, Catarina Lopes-Dias, Gernot R Müller-Putz, and Motoaki Kawanabe. On the interpretation of linear riemannian tangent space model parameters in m/eeg. In *2021 43rd Annual International Conference of the IEEE Engineering in Medicine & Biology Society (EMBC)*, pp. 5909–5913. IEEE, 2021.

Reinmar J. Kobler, Jun-ichiro Hirayama, and Motoaki Kawanabe. Controlling The Fréchet Variance Improves Batch Normalization on the Symmetric Positive Definite Manifold. In *ICASSP 2022 - 2022 IEEE International Conference on Acoustics, Speech and Signal Processing (ICASSP)*, pp. 3863–3867, Singapore, Singapore, 2022b. IEEE. doi: 10.1109/ICASSP43922.2022.9746629.

Max Kochurov, Rasul Karimov, and Serge Kozlukov. Geoopt: Riemannian optimization in pytorch. *arXiv preprint arXiv:2005.02819*, 2020.

Robert Leeb, Felix Lee, Claudia Keinrath, Reinhold Scherer, Horst Bischof, and Gert Pfurtscheller. Brain–computer communication: motivation, aim, and impact of exploring a virtual apartment. *IEEE Transactions on Neural Systems and Rehabilitation Engineering*, 15(4):473–482, 2007. doi: 10.1109/TNSRE.2007.906956.

Siyang Li, Ziwei Wang, Hanbin Luo, Lieyun Ding, and Dongrui Wu. T-time: Test-time information maximization ensemble for plug-and-play bcis. *IEEE Transactions on Biomedical Engineering*, 2023. doi: 10.1109/TBME.2023.3303289.

Xinhao Li, Jingjing Li, Lei Zhu, Guoqing Wang, and Zi Huang. Imbalanced source-free domain adaptation. In *Proceedings of the 29th ACM international conference on multimedia*, pp. 3330–3339, 2021.

Jian Liang, Dapeng Hu, and Jiashi Feng. Do we really need to access the source data? source hypothesis transfer for unsupervised domain adaptation. In *International conference on machine learning*, pp. 6028–6039. PMLR, 2020.

Jian Liang, Ran He, and Tieniu Tan. A Comprehensive Survey on Test-Time Adaptation Under Distribution Shifts. *International Journal of Computer Vision*, July 2024. doi: 10.1007/s11263-024-02181-w.

Yuang Liu, Wei Zhang, and Jun Wang. Source-free domain adaptation for semantic segmentation. In *Proceedings of the IEEE/CVF Conference on Computer Vision and Pattern Recognition*, pp. 1215–1224, 2021.

Fabien Lotte, Laurent Bougrain, Andrzej Cichocki, Maureen Clerc, Marco Congedo, Alain Rakotomamonjy, and Florian Yger. A review of classification algorithms for eeg-based brain–computer interfaces: a 10 year update. *Journal of neural engineering*, 15(3):031005, 2018. doi: 10.1088/1741-2552/aab2f2.

Apolline Mellot, Antoine Collas, Pedro LC Rodrigues, Denis Engemann, and Alexandre Gramfort. Harmonizing and aligning m/eeg datasets with covariance-based techniques to enhance predictive regression modeling. *Imaging Neuroscience*, 1:1–23, 2023. doi: 10.1162/imag\_a\_00040.

Apolline Mellot, Antoine Collas, Sylvain Chevallier, Alexandre Gramfort, and Denis A Engemann. Geodesic optimization for predictive shift adaptation on eeg data. *arXiv preprint arXiv:2407.03878*, 2024.

Maher Moakher. A Differential Geometric Approach to the Geometric Mean of Symmetric Positive-Definite Matrices. *SIAM Journal on Matrix Analysis and Applications*, 26(3):735–747, 2005. doi: 10.1137/S0895479803436937.

Ernst Niedermeyer and FH Lopes da Silva. *Electroencephalography: basic principles, clinical applications, and related fields*. Lippincott Williams & Wilkins, 2005. ISBN 978-0190228484.

Paul L Nunez and Ramesh Srinivasan. *Electric fields of the brain: the neurophysics of EEG*. Oxford University Press, USA, 2006. ISBN 9780195050387.

Adam Paszke, Sam Gross, Francisco Massa, Adam Lerer, James Bradbury, Gregory Chanan, Trevor Killeen, Zeming Lin, Natalia Gimelshein, Luca Antiga, et al. Pytorch: An imperative style, high-performance deep learning library. *Advances in neural information processing systems*, 32, 2019.

Fabian Pedregosa, Gaël Varoquaux, Alexandre Gramfort, Vincent Michel, Bertrand Thirion, Olivier Grisel, Mathieu Blondel, Peter Prettenhofer, Ron Weiss, Vincent Dubourg, et al. Scikit-learn: Machine learning in python. *the Journal of machine Learning research*, 12:2825–2830, 2011. doi: 10.5555/1953048.2078195.

Xavier Pennec. Barycentric subspace analysis on manifolds. *The Annals of Statistics*, 46, 2018. doi: 10.1214/17-AOS1636.

Ignacio Perez-Pozuelo, Bing Zhai, Joao Palotti, Raghvendra Mall, Michaël Aupetit, Juan M Garcia-Gomez, Shahrad Taheri, Yu Guan, and Luis Fernandez-Luque. The future of sleep health: a data-driven revolution in sleep science and medicine. *NPJ digital medicine*, 3(1):42, 2020. doi: 10.1038/s41746-020-0244-4.

Mathias Perslev, Sune Darkner, Lykke Kempfner, Miki Nikolic, Poul Jørgen Jennum, and Christian Igel. U-sleep: resilient high-frequency sleep staging. *NPJ digital medicine*, 4(1):72, 2021. doi: 10.1038/s41746-021-00440-5.

Gert Pfurtscheller and FH Lopes Da Silva. Event-related eeg/meg synchronization and desynchronization: basic principles. *Clinical neurophysiology*, 110(11):1842–1857, 1999. doi: 10.1016/s1388-2457(99)00141-8.

Pedro Luiz Coelho Rodrigues, Christian Jutten, and Marco Congedo. Riemannian Procrustes Analysis: Transfer Learning for Brain–Computer Interfaces. *IEEE Transactions on Biomedical Engineering*, 66(8):2390–2401, 2019. doi: 10.1109/TBME.2018.2889705.

Raphaëlle N. Roy, Marcel F. Hinss, Ludovic Darmet, Simon Ladouce, Emilie S. Jahanpour, Bertille Somon, Xiaoqi Xu, Nicolas Drougard, Frédéric Dehais, and Fabien Lotte. Retrospective on the First Passive Brain-Computer Interface Competition on Cross-Session Workload Estimation. *Frontiers in Neuroergonomics*, 3:838342, 2022. doi: 10.3389/fnrgo.2022.838342.

David Sabbagh, Pierre Ablin, Gaël Varoquaux, Alexandre Gramfort, and Denis A Engemann. Predictive regression modeling with meg/eeg: from source power to signals and cognitive states. *NeuroImage*, 222:116893, 2020. doi: j.neuroimage.2020.116893.

Robin Tibor Schirrmeister, Jost Tobias Springenberg, Lukas Dominique Josef Fiederer, Martin Glasstetter, Katharina Eggensperger, Michael Tangermann, Frank Hutter, Wolfram Burgard, and Tonio Ball. Deep learning with convolutional neural networks for eeg decoding and visualization. *Human Brain Mapping*, aug 2017. ISSN 1097-0193. doi: 10.1002/hbm.23730. URL <http://dx.doi.org/10.1002/hbm.23730>.

Yuan Shi and Fei Sha. Information-theoretical learning of discriminative clusters for unsupervised domain adaptation. In *Proceedings of the 29th International Conference on International Conference on Machine Learning*, pp. 1275–1282, Madison, WI, USA, 2012. Omnipress.

Nazmi Sofian Suhaimi, James Mountstephens, and Jason Teo. Eeg-based emotion recognition: a state-of-the-art review of current trends and opportunities. *Computational intelligence and neuroscience*, 2020(1):8875426, 2020. doi: 10.1155/2020/8875426.

Michael Tangermann, Klaus-Robert Müller, Ad Aertsen, Niels Birbaumer, Christoph Braun, Clemens Brunner, Robert Leeb, Carsten Mehring, Kai J Miller, Gernot R Müller-Putz, et al. Review of the bci competition iv. *Frontiers in neuroscience*, 6:55, 2012. doi: 10.3389/fnins.2012.00055.

Mario Giovanni Terzano, Liborio Parrino, Adriano Sherieri, Ronald Chervin, Sudhansu Chokroverty, Christian Guilleminault, Max Hirshkowitz, Mark Mahowald, Harvey Moldofsky, Agostino Rosa, et al. Atlas, rules, and recording techniques for the scoring of cyclic alternating pattern (cap) in human sleep. *Sleep medicine*, 2(6):537–554, 2001. doi: 10.1016/s1389-9457(01)00149-6.

Philipp Thölke, Yorguin-Jose Mantilla-Ramos, Hamza Abdelhedi, Charlotte Maschke, Arthur Deghan, Yann Harel, Anirudha Kemtur, Loubna Mekki Berrada, Myriam Sahraoui, Tammy Young, et al. Class imbalance should not throw you off balance: Choosing the right classifiers and performance metrics for brain decoding with imbalanced data. *NeuroImage*, 277:120253, 2023. doi: 10.1016/j.neuroimage.2023.120253.

Xiaoxi Wei, A. Aldo Faisal, Moritz Grosse-Wentrup, Alexandre Gramfort, Sylvain Chevallier, Vinay Jayaram, Camille Jeunet, Stylianos Bakas, Siegfried Ludwig, Konstantinos Barmpas, Mehdi Bahri, Yannis Panagakis, Nikolaos Laskaris, Dimitrios A. Adamos, Stefanos Zafeiriou, William C. Duong, Stephen M. Gordon, Vernon J. Lawhern, Maciej Śliwowski, Vincent Rouanne, and Piotr Tempczyk. 2021 BEETL Competition: Advancing Transfer Learning for Subject Independence and Heterogenous EEG Data Sets. In Douwe Kiela, Marco Ciccone, and Barbara Caputo (eds.), *Proceedings of the NeurIPS 2021 Competitions and Demonstrations Track*, volume 176 of *Proceedings of Machine Learning Research*, pp. 205–219. PMLR, 2022.

Jonathan R Wolpaw, Niels Birbaumer, Dennis J McFarland, Gert Pfurtscheller, and Theresa M Vaughan. Brain–computer interfaces for communication and control. *Clinical neurophysiology*, 113(6):767–791, 2002. doi: 10.1016/S1388-2457(02)00057-3.

Edward A Wolpert. A manual of standardized terminology, techniques and scoring system for sleep stages of human subjects. *Archives of General Psychiatry*, 20(2):246–247, 1969. doi: 10.1001/archpsyc.1969.01740140118016.

Dongrui Wu, Yifan Xu, and Bao-Liang Lu. Transfer learning for eeg-based brain–computer interfaces: A review of progress made since 2016. *IEEE Transactions on Cognitive and Developmental Systems*, 14(1):4–19, 2020. doi: 10.1109/TCDS.2020.3007453.

Or Yair, Mirela Ben-Chen, and Ronen Talmon. Parallel transport on the cone manifold of spd matrices for domain adaptation. *IEEE Transactions on Signal Processing*, 67(7):1797–1811, 2019. doi: 10.1109/TSP.2019.2894801.

Shiqi Yang, Yaxing Wang, Joost Van De Weijer, Luis Herranz, and Shangling Jui. Generalized source-free domain adaptation. In *Proceedings of the IEEE/CVF international conference on computer vision*, pp. 8978–8987, 2021.

Paolo Zanini, Marco Congedo, Christian Jutten, Salem Said, and Yannick Berthoumieu. Transfer learning: A riemannian geometry framework with applications to brain–computer interfaces. *IEEE Transactions on Biomedical Engineering*, 65(5):1107–1116, 2017. doi: 10.1109/TBME.2017.2742541.

Bangyan Zhou, Xiaopei Wu, Zhao Lv, Lei Zhang, and Xiaojin Guo. A fully automated trial selection method for optimization of motor imagery based brain-computer interface. *PloS one*, 11(9):e0162657, 2016. doi: 10.1371/journal.pone.0162657.

## A APPENDIX

### A.1 PROOF OF PROPOSITION 1

Proposition 1 stats that given the generative model specified in section 3.1 and a set of examples  $\mathcal{E}_j = \{(E_i, y_i, j) | E_i \in \mathcal{S}_P^+, y_i \in \mathcal{Y}\}_{i \leq M_j}$  of domain  $j \in \mathcal{J}$ , we have that the Fréchet mean of  $\mathcal{E}_j$ , defined in (2), converges with  $M_j \rightarrow \infty$  to the identity matrix  $I_P$  for all domains  $j \in \mathcal{J}$ .

Since  $(\mathcal{S}_P^+, g^{\text{AIRM}})$  forms a Cartan-Hadamard manifold with global non-positive sectional curvature, a unique Fréchet mean exists (Bhatia, 2013). At the global minimum, we have:

$$0 \stackrel{!}{=} \nabla_E \nu_E(\mathcal{E}_j) = \nabla_E \frac{1}{M_j} \sum_{i=1}^{M_j} \delta^2(E, E_i) = \frac{1}{M_j} \sum_{i=1}^{M_j} \nabla_E \delta^2(E, E_i) = -\frac{1}{M_j} \sum_{i=1}^{M_j} \text{Log}_E(E_i) \quad (22)$$

$$= -\frac{1}{M_j} \sum_{i=1}^{M_j} E^{\frac{1}{2}} \log(E^{-\frac{1}{2}} E_i E^{-\frac{1}{2}}) E^{\frac{1}{2}} = -\frac{1}{M_j} E^{\frac{1}{2}} \left( \sum_{i=1}^{M_j} \log(E^{-\frac{1}{2}} E_i E^{-\frac{1}{2}}) \right) E^{\frac{1}{2}} \quad (23)$$

$$0 \stackrel{!}{=} \sum_{i=1}^{M_j} \log(E^{-\frac{1}{2}} E_i E^{-\frac{1}{2}}) \quad (24)$$

where we used the derivative of the Riemannian distance (Moakher, 2005; Pennec, 2018) in (22). For  $E = I_P$ , (24) simplifies to:

$$\sum_{i=1}^{M_j} \log(E_i) \stackrel{!}{=} 0 \xrightarrow{M_j \rightarrow \infty} \mathbb{E}\{\log(E_i)\} \stackrel{!}{=} 0 \quad (25)$$

$$\mathbb{E}\{B\tilde{y}_i + \varepsilon_i\} = B\mathbb{E}\{\tilde{y}_i\} + \mathbb{E}\{\varepsilon_i\} \stackrel{!}{=} 0 \quad (26)$$

which holds true because by definition  $\tilde{y}_i$  and  $\varepsilon_i$  are zero-mean. Therefore,  $E_j = I_P$  is the global minimizer of  $\nu_E(\mathcal{E}_j)$  for all domains  $j \in \mathcal{J}$ .  $\square$

### A.2 PROOF OF PROPOSITION 2

Proposition 2 states that for the generative model, specified in section 3.1, RCT+TSM compensates conditional distribution shifts introduced by the invertible linear map  $A_j$ , defined in (8), and recovers domain-invariant representations if there are no target shifts (i.e.,  $p_j(y=y) = p(y=y) \forall y \in \mathcal{Y}, \forall j \in \mathcal{J}_s \cup \mathcal{J}_t$ ).

Due to the congruence invariance of the Fréchet mean (Bhatia, 2013) we have

$$\bar{C}_j = \arg \min_{G \in \mathcal{S}_P^+} \nu_G(\mathcal{C}_j) = A_j \bar{E}_j A_j^T \quad (27)$$

where  $\bar{E}_j$  is the Fréchet mean of  $\mathcal{E}_j$ . Utilizing proposition 1 (i.e.,  $\bar{E}_j = I_P \forall j$ ) and plugging in (9) for  $A_j$ , (27) simplifies to:

$$\bar{C}_j = A_j I_P A_j^T = Q \exp(P_j) \exp(P_j) Q^T = Q \exp(P_j)^2 Q^T \quad (28)$$

$$\Rightarrow \bar{C}_j^{-\frac{1}{2}} = Q \exp(P_j)^{-1} Q^T \quad (29)$$

The RCT+TSM transform, as defined in (14), recenters the data  $C_i \in \mathcal{C}_j$  for each domain  $j$ . Excluding the invertible mapping upper, RCT+TSM computes:

$$\log \left( \bar{C}_j^{-\frac{1}{2}} C_i \bar{C}_j^{-\frac{1}{2}} \right) = \log (Q \exp(P_j)^{-1} Q^T C_i Q \exp(P_j)^{-1} Q^T) \quad (30)$$

$$= \log (Q \exp(P_j)^{-1} A_j E_i A_j^T \exp(P_j)^{-1} Q^T) \quad (31)$$

$$= \log (Q \exp(P_j)^{-1} Q^T Q \exp(P_j) E_i \exp(P_j) Q^T Q \exp(P_j)^{-1} Q^T) \quad (32)$$

$$= \log (Q E_i Q^T) = Q \log(E_i) Q^T \quad (33)$$

where we used (13) for  $C_i$ , the fact that  $Q$  is an orthogonal matrix and  $\log(ACA^{-1}) = A\log(C)A^{-1}$  for non-singular  $A$  and  $C \in \mathcal{S}_P^+$ . Plugging (11) for  $\log(E_i)$ , we obtain a direct relationship to the label  $y_i$  via  $\tilde{y}_i$

$$\log \left( \bar{C}_j^{-\frac{1}{2}} C_i \bar{C}_j^{-\frac{1}{2}} \right) = Q_{\text{upper}}^{-1} (B \tilde{y}_i + \varepsilon_i) Q^T \quad (34)$$

$$= Q_{\text{upper}}^{-1} (B (1_{y_i} - \bar{y}_j) + \varepsilon_i) Q^T \quad (35)$$

where the vector  $\bar{y}_j = [p_j(y=y_k)]_{k=1, \dots, |\mathcal{Y}|}$  contains the class priors for domain  $j$ . If there are no target shifts the class priors are constant  $p_j(y=y) = p(y=y) \forall y \in \mathcal{Y}$  for all domains  $j \in \mathcal{J}_s \cup \mathcal{J}_t$ , and consequently  $\bar{y}_j = \bar{y}$ . Then (35) simplifies to:

$$\log \left( \bar{C}_j^{-\frac{1}{2}} C_i \bar{C}_j^{-\frac{1}{2}} \right) = Q_{\text{upper}}^{-1} (B (1_{y_i} - \bar{y}) + \varepsilon_i) Q^T \quad (36)$$

which contains only domain-invariant terms on the right hand side. Thus, RCT+TSM compensates the conditional shifts introduced by  $A_j$ .  $\square$

### A.3 SLEEP STAGE DATASET DETAILS

Dataset	Recordings	Subjects	Channel numbers	Patients	Scorer	Scoring rule
ISRUC-SG1	100	100	6	✓	Scorer1	AASM
ISRUC-SG2	16	8	6	✓	Scorer1	AASM
ISRUC-SG3	10	10	6	✗	Scorer1	AASM
Dreem-SG1	22	22	12	✗	Scorer1	AASM
Dreem-SG2	50	50	8	✓	Scorer1	AASM
HMC	154	154	4	✓	-	AASM
CAP-SG1	36	36	13	✓	-	K&M
CAP-SG2	34	34	9	✓	-	K&M
CAP-SG3	22	22	5	✓	-	K&M

Table A1: **Sleep stage dataset details.** Overview of datasets and their subgroups (SG), including the number of recordings, subjects, channel numbers, patient status, scorer (the chosen scorer if there are multiple scorers), and scoring rule.

## A.4 EEG-BASED SLEEP STAGING RESULTS

Model	SFUDA	Dataset:	CAP		Dreem		HMC		ISRUC		Overall	
			Group:		patient (n=82)	healthy (n=22)	patient (n=50)	patient (n=154)	healthy (n=10)	patient (n=108)	healthy (n=32)	patient (n=394)
			mean	std	t-val	mean	std	t-val	mean	std	mean	std
Chambon	w/o	mean	64.7	65.2	53.4	64.0	72.7	68.9	67.5	64.2		
		std	10.7	9.1	16.2	9.6	3.9	8.2	8.6	11.5		
		t-val	• -6.8	• -5.3	• -6.1	• -7.0	-2.6	• -4.6	• -5.8	• -11.3		
USleep	w/o	mean	59.1	55.9	48.4	66.6	72.9	68.8	61.3	63.3		
		std	10.3	8.3	8.2	9.3	6.1	8.3	11.0	11.3		
		t-val	• -12.1	• -8.0	• -13.3	• -2.8	-2.2	• -4.3	• -6.8	• -12.1		
TSMNet	w/o	mean	68.0	65.9	66.7	63.6	73.4	68.7	68.3	66.3		
		std	11.2	9.6	12.4	11.3	3.9	9.3	8.9	11.1		
		t-val	• -3.7	• -6.5	-1.0	• -6.8	-3.4	• -3.8	• -7.0	• -8.2		
RCT		mean	68.2	68.9	64.2	62.2	72.8	66.6	70.1	64.9		
		std	8.8	5.8	8.5	6.0	2.8	6.4	5.3	7.5		
		t-val	• -6.3	• -4.8	• -8.6	• -15.3	• -3.8	• -13.4	• -6.2	• -21.4		
SPDIM (geodesic)		mean	68.6	70.0	66.8	64.7	74.6	68.3	71.4	66.8		
		std	9.2	6.6	9.0	7.1	3.2	6.4	6.1	7.8		
		t-val	• -6.4	• -3.9	• -3.7	• -12.2	• -3.9	• -10.0	• -5.3	• -16.8		
SPDIM (bias) <i>proposed</i>		mean	71.0	72.1	68.1	68.6	76.7	71.6	73.5	69.9		
		std	9.6	8.0	9.8	8.5	3.4	6.9	7.2	8.6		
		t-val	-	-	-	-	-	-	-	-		
IM classifier (bias)		mean	69.8	70.3	65.7	64.1	74.7	68.9	71.7	66.8		
		std	9.5	6.8	9.2	6.9	2.7	6.8	6.1	8.1		
		t-val	• -3.3	• -4.0	• -7.4	• -13.0	• -3.9	• -8.1	• -5.4	• -15.6		
IM (classifier)		mean	67.4	68.8	63.1	62.3	73.2	67.7	70.2	64.9		
		std	10.5	8.5	10.9	9.8	5.0	8.8	7.7	10.1		
		t-val	• -5.9	• -3.1	• -6.1	• -14.5	• -3.8	• -8.6	• -4.3	• -18.0		
IM (all)		mean	54.8	46.9	36.2	35.8	53.6	45.9	49.0	42.5		
		std	14.8	13.8	11.4	11.2	13.4	12.5	13.8	14.5		
		t-val	• -13.3	• -9.6	• -17.1	• -32.8	• -6.4	• -23.0	• -11.6	• -39.9		

Table A2: **Sleep-staging results per dataset.** Average and standard deviation of test-set scores (balanced accuracy; higher is better) across public sleep staging datasets. For all IM and SPDIM variants, the parameters that were tuned to the test-data with the IM loss are indicated in brackets. Permutation-paired t-tests were used to identify significant differences between our *proposed* (i.e., TSMNet+SPDIM(bias)) and baseline methods (1e4 permutations, 8 tests, t-max correction). Student's t values summarize the effect strength. Significant differences are highlighted ( $\bullet p \leq 0.05$ ,  $\bullet p \leq 0.01$ ,  $\bullet p \leq 0.001$ ).

## A.5 EEG-BASED MOTOR IMAGERY BCI

IR	SFUDA	Evaluation :			session	Overall	subject				Overall	
		Dataset	2014001 (n=9)	2014004 (n=9)	2015001 (n=12)	Zhou2016 (n=4)	2014001 (n=9)	2014004 (n=9)	2015001 (n=12)	Zhou2016 (n=4)		
0.2	w/o	mean	68.6	74.8	82.7	81.0	76.7	41.1	69.5	61.1	77.8	60.0
		std	12.9	11.1	13.4	2.5	12.8	12.7	9.6	10.9	2.6	16.2
		t-val	-0.5	0.4	-0.6	-1.8	-0.9	• -4.3	-1.5	-2.0	-1.3	• -3.5
RCT	RCT	mean	69.3	73.5	81.2	80.6	76.0	52.1	69.6	71.5	76.2	66.4
		std	16.2	11.0	8.6	2.4	12.0	13.9	9.8	13.5	3.1	14.5
		t-val	-0.3	-0.9	-2.4	-7.0	• -2.8	-0.3	-1.9	-2.6	-1.9	• -3.2
SPDIM (geodesic)	SPDIM (geodesic)	mean	70.0	74.7	83.7	82.6	77.6	52.3	70.9	73.4	78.4	67.7
		std	16.5	11.9	10.3	3.5	13.1	15.1	10.9	15.2	3.6	16.0
		t-val	0.4	0.8	0.1	-1.4	0.1	-0.3	-1.4	-0.3	-1.1	-1.6
SPDIM (bias)	SPDIM (bias)	mean	69.7	74.3	83.6	84.1	77.5	52.6	72.2	73.6	80.4	68.5
		std	18.4	12.2	10.6	2.2	13.9	16.5	12.0	14.8	2.4	16.6
		t-val	-	-	-	-	-	-	-	-	-	-
IM (classifier bias)	IM (classifier bias)	mean	69.9	74.2	83.2	78.3	76.7	52.9	70.6	73.0	75.4	67.3
		std	17.5	12.5	10.1	3.0	13.3	15.0	9.9	15.1	3.8	15.3
		t-val	0.2	-0.0	-0.6	-11.2	-1.7	0.4	-1.0	-0.7	-1.7	-1.7
IM (classifier)	IM (classifier)	mean	66.6	70.9	78.2	77.0	73.0	50.5	67.0	69.7	69.0	63.8
		std	17.2	9.5	6.6	1.7	11.5	14.9	9.1	12.4	7.5	14.1
		t-val	-3.1	-3.0	• -3.8	-17.2	• -6.8	-1.1	• -4.1	• -3.9	-2.9	• -5.0
IM (all)	IM (all)	mean	37.9	50.9	70.8	55.4	55.0	36.0	50.4	63.2	56.0	51.8
		std	10.9	1.7	7.8	6.4	15.1	7.5	1.7	8.3	4.1	12.5
		t-val	• -6.6	• -6.1	• -4.0	-7.5	• -9.5	• -4.0	• -5.2	-2.5	-10.3	• -7.3
1.0	RCT	mean	73.7	77.4	85.3	84.6	80.0	54.6	73.3	74.3	80.9	69.6
		std	15.3	12.5	10.4	2.3	12.5	16.1	11.1	14.7	1.5	15.9
		t-val	3.6	• 3.9	2.6	0.6	• 5.4	1.9	1.1	0.8	0.6	2.3

Table A3: **Motor imagery BCI results per dataset.** Average and standard deviation of test-set scores (balanced accuracy; higher is better) across public motor imagery BCI datasets. For all IM and SPDIM variants, the parameters that were tuned to the test-data with the IM loss are indicated in brackets. Permutation-paired t-tests were used to identify significant differences between the *proposed* (i.e., TSMNet+SPDIM(bias)) and baseline methods (1e4 permutations, 7 tests, t-max correction). Student’s t values summarize the effect strength. Significant differences are highlighted ( $\cdot p \leq 0.05$ ,  $\bullet p \leq 0.01$ ,  $\bullet\bullet p \leq 0.001$ ).